

Tight-binding equations for longitudinally driven waveguides: Lieb and Kagome lattices

Mark J. Ablowitz and Justin T. Cole¹

¹*Department of Applied Mathematics, University of Colorado, Boulder, Colorado 80309*

(Dated: August 24, 2022)

A tight-binding approximation is developed for longitudinally driven photonic lattices with three lattice sites per unit cell. Two cases are considered in detail: Lieb and Kagome lattices. The lattice is decomposed into three sublattices each of which are allowed move independently of one another. Emphasis is placed on periodic driving induced by laser-etched helical coils along the direction of propagation. The linear Floquet bands are constructed for various sublattice rotation patterns such as: phase offset, different radii, different frequency, and a quasi one-dimensional motion. Depending on the nature of the band structure, edge states can move unidirectionally. In this case they move effectively across defects due to underlying topological protection. On the other hand, non-topological edge waves are found to reflect off defects.

PACS numbers: 42.65.Tg, 42.65.Jx, 42.82.Et

I. INTRODUCTION

The study of photonic topological insulators has received considerable interest due in part to their remarkable mode propagation properties. In photonic systems, breaking time-reversal symmetry has been shown to support topologically protected states [1]. These modes manifest themselves in edge states that travel in one direction and propagate stably and without scatter around defects.

The first experimental realization of a topologically protected electromagnetic wave was observed in [2]. In that work an external magnetic field was applied to a periodic array of ferrite rods in order to break time-reversal symmetry. It was shown that microwaves could be localized along the device boundary, move unidirectionally, and propagate scatter-free around barrier defects.

In photonics, an experimental realization of a topologically protected system was presented in [3]. In this work time-reversal symmetry was broken by a honeycomb array of helically-varying waveguides etched into a bulk medium. In spatial optics the direction of propagation plays the role of time and so the helical variations act as a time-dependent potential. In [3] the lattice, which consists of two sublattices, was restricted to rotate uniformly in the direction of propagation. This paper also focuses on a system of helically-varying waveguides however here we allow each sublattice to i) move independently and ii) consider more than two sublattices. In prior work we studied two sublattice systems: honeycomb and square lattices [4].

Longitudinally varying waveguide arrays have been used to explore numerous other topological systems. Linear and nonlinear staggered square arrangements were considered in [5] and [6], respectively. By introducing a phase offset among the sublattice waveguides it is possible to observe a phase transition point known as a conical Weyl point [7]. For intense nonlinear beams the edge mode envelope has been found to be governed by a nonlinear Schrödinger equation and, in certain parameter regimes, support topologically protected edge solitons [4]

as well as exhibit modulational instability [8]. Unidirectional edge modes have also been observed to propagate in helically-driven quasicrystals [9]; i.e. structures that are not periodic but contain some long range order.

Photonic topological systems have potential to act as optical isolators (one-way transmitters) [10, 11] and circulators [12]. Photonic topological insulator systems have also been found to generate and support novel and robust laser systems [13–17]. Properties and evolution of nonlinear topological edge states were investigated in [4] and [18].

In [4] a systematic approach to derive tight-binding models in honeycomb and square lattices (two lattice sites per unit cell) was developed. This paper extends those methods to more complex (three lattice sites per unit cell) periodically driven arrays. In particular, we focus on the Lieb and Kagome lattices. In the absence of external driving these lattices can support localized flat band modes in the bulk [19–22] or along the edge [19, 23]. Interestingly, flat band modes can be diffraction-free [24].

Introducing uniform helical variation to a Lieb waveguide array has been shown to offer a rich set of edge mode dynamics [23]. These include the presence of a (stationary) flat band mode, as well as (traveling) topologically protected modes. In the course of propagation these traveling modes may interact with the flat band modes at certain mode frequencies. Here we generalize the work considered in [23] to allow more complex sublattice rotation patterns. To our knowledge, edge mode dynamics for helically driven Kagome lattices have been studied much less than the Lieb lattice.

In this work we decompose the Lieb and Kagome lattice into three sublattices that can move independently of each other. Each of these sublattices is driven in a periodic fashion along the direction of propagation. We derive a tight-binding system, valid in a deep lattice limit, that describes incoming light beams. This model takes into account the lattice driving via periodic functions that are parametrized in terms of the direction of propagation, i.e. the “time” variable. As a result, we derive a system with periodic coefficients of which we

compute the Floquet bands and the corresponding edge eigenmodes they support. We also briefly consider nonlinear edge modes that exhibit properties of topologically protection.

A. Paraxial Wave Equation

The propagation of intense, paraxial light beams in Kerr waveguide arrays is well-known to be governed by the nonlinear Schrödinger (NLS) equation

$$i\frac{\partial\psi}{\partial z} + \frac{1}{2k_0}\nabla^2\psi - \frac{k_0}{n_0}(n_\ell(\mathbf{r}, z) - n_2|\psi|^2)\psi = 0, \quad (1)$$

where k_0 is the carrier wavenumber, n_0 is the bulk media index of refraction, and $\nabla^2 \equiv \partial_x^2 + \partial_y^2$. The complex electric field envelope $\psi(\mathbf{r}, z)$ depends on the position in both the direction of propagation, z , and the transverse plane, $\mathbf{r} = (x, y)$. Well-separated regions of high refractive index are carved into bulk media using a femtosecond laser etching process [25]. The presence of these lattice waveguides is represented by the potential function $-n_\ell(\mathbf{r}, z)$. Additionally, focusing Kerr nonlinear media ($n_2 > 0$) exhibits an intensity-dependent response to the incoming light beam. It is directly from equation (1) that we derive our tight-binding equations.

In this paper we restrict our attention to non-simple lattices with three lattice sites (a, b, c) per unit cell. To model such a scenario, we rewrite the lattice potential as the combination of three interpenetrating sublattices

$$n_\ell(\mathbf{r}, z) = |\Delta n| \left[1 - V_a(\mathbf{r}, z) - V_b(\mathbf{r}, z) - V_c(\mathbf{r}, z) \right],$$

where $|\Delta n|$ denotes the contrast in waveguide refractive index from the bulk media. Each sublattice is taken to consist of a sum of Gaussian functions

$$V_j(\mathbf{r}, z) = \sum_{\mathbf{v} \in \mathcal{R}_j} \tilde{V}(\mathbf{r} - \mathbf{v} - \mathbf{h}_j(z)), \quad j = a, b, c \quad (2)$$

$$\tilde{V}(\mathbf{r}) = \exp\left(-\frac{x^2}{\sigma_x^2} - \frac{y^2}{\sigma_y^2}\right),$$

for $\sigma_x, \sigma_y > 0$. The Gaussian peaks of V_j (in the absence of rotation) are located at lattice sites shown in Figs. 1 and 2.

The zeros of the lattice potential correspond to the center of the waveguides where the index of refraction is largest. The smooth parametric functions $\mathbf{h}_j(z)$ drive the sublattices. The parameters σ_x, σ_y control the geometric shape of the waveguides. When $\sigma_x = \sigma_y$ the waveguides are circular (isotropic), whereas the waveguides are elliptical (anisotropic) when $\sigma_x \neq \sigma_y$.

Here we concentrate on driving functions which are periodic in z . Specifically, we examine

$$\mathbf{h}_j(z) = R_j (\cos(\Lambda_j z + \chi_j), \sin(\Lambda_j z + \chi_j)), \quad (3)$$

where R_j is the helix radius, Ω_j is the angular frequency, and χ_j is an arbitrary phase shift. It is useful to transform to a coordinate frame co-moving with the $V_b(\mathbf{r}, z)$

sublattice by performing the change of variable

$$\tilde{\mathbf{r}} = \mathbf{r} - \mathbf{h}_b(z), \quad \tilde{z} = z.$$

Introducing the transformation

$$\psi(\mathbf{r}, z) = \tilde{\psi}(\tilde{\mathbf{r}}, \tilde{z}) \exp\left(\frac{-i \int_0^{\tilde{z}} |\mathbf{A}(\zeta)|^2 d\zeta}{2}\right),$$

for the pseudo-field (vector potential)

$$\mathbf{A}(\tilde{z}) = -k_0 \mathbf{h}'_b(\tilde{z}),$$

we get (after dropping the tilde notation)

$$i\frac{\partial\psi}{\partial z} + \frac{1}{2k_0}(\nabla + i\mathbf{A}(z))^2\psi - \frac{k_0}{n_0}(n_\ell(\mathbf{r}, z) - n_2|\psi|^2)\psi = 0. \quad (4)$$

This equation is nondimensionalized by

$$x = \ell x', \quad y = \ell y', \quad z = z_* z',$$

$$\sigma_x = \ell \sigma'_x, \quad \sigma_y = \ell \sigma'_y, \quad \psi = \sqrt{I_*} \psi',$$

where ℓ is the distance between nearest neighbor lattice sites, $z_* = 2k_0 \ell^2$ is a typical propagation distance, I_* is the peak intensity of the input beam, $\gamma = 2k_0^2 \ell^2 n_2 I_*/n_0 > 0$ is the nonlinearity coefficient, and $V_0^2 = 2k_0^2 \ell^2 |\Delta n|/n_0$ is the amplitude of the potential, which we assume is large. Dropping the prime notation, gives the dimensionless equation

$$i\frac{\partial\psi}{\partial z} + (\nabla + i\mathbf{A}(z))^2\psi - V(\mathbf{r}, z)\psi + \gamma|\psi|^2\psi = 0, \quad (5)$$

with potential function

$$V(\mathbf{r}, z) = V_0^2 \left[1 - V_a(\mathbf{r} - \Delta\mathbf{h}_{ab}(z)) - V_b(\mathbf{r}) - V_c(\mathbf{r} - \Delta\mathbf{h}_{cb}(z)) \right],$$

where

$$\Delta\mathbf{h}_{ij}(z) \equiv \mathbf{h}_i(z) - \mathbf{h}_j(z) \quad i, j = a, b, c. \quad (6)$$

In dimensionless form, the driving functions are

$$\mathbf{h}_j(z) = \eta_j (\cos(\Omega_j z + \chi_j), \sin(\Omega_j z + \chi_j)), \quad j = a, b, c$$

where $\eta_j = R_j/\ell$ and $\Omega_j = \Lambda_j z_*$.

Finally, we introduce the phase transformation

$$\psi(\mathbf{r}, z) = \phi(\mathbf{r}, z) e^{-i\mathbf{r} \cdot \mathbf{A}(z)},$$

which simplifies the above equation to

$$i\frac{\partial\phi}{\partial z} + \nabla^2\phi + \mathbf{r} \cdot \mathbf{A}_z\phi - V(\mathbf{r}, z)\phi + \gamma|\phi|^2\phi = 0. \quad (7)$$

The pseudo-field in dimensionless coordinates is given by

$$\mathbf{A}(z) = \kappa (\sin(\Omega_b z + \chi_b), -\cos(\Omega_b z + \chi_b)), \quad (8)$$

(since we are working in the $\mathbf{h}_b(z)$ reference frame) where $\kappa = k_0 \ell R_b \Lambda_b$.

II. TIGHT-BINDING APPROXIMATION

We now develop a tight-binding approximation from Eq. (7). This tight-binding model requires the contrast in the refractive index between the waveguide and background media to be sharp; this means that nearest neighbor interactions are dominant. As a result, we are working in a deep lattice regime; i.e. $V_0^2 \gg 1$. In addition, locally we approximate the lattice potential by a helically-varying paraboloid potential. As such, we represent the beam field $\phi(\mathbf{r}, z)$ by a sum of strongly decaying orbital functions centered at the (z -dependent) lattice sites. The localized orbital modes are taken to satisfy a harmonic oscillator equation with quadratic potential function that is periodic in z . Furthermore, as mentioned above, in the tight-binding limit these modes are well-localized so that the only significant interactions occur between nearest neighbors.

Near the well-separated lattice minima we approximate the potential by the first few terms of its Taylor series. The local approximation of the potential is the paraboloid

$$\bar{V}(\mathbf{r}) = V_0^2 \left(\frac{x^2}{\sigma_x^2} + \frac{y^2}{\sigma_y^2} \right), \quad (9)$$

nearby the rotating lattice sites. Near here the wave field is taken to satisfy the orbital equation

$$[-\nabla^2 + \bar{V}(\mathbf{r} - \mathbf{v} - \Delta \mathbf{h}_{jb}(z))] \phi_{j,\mathbf{v}} = E \phi_{j,\mathbf{v}}, \quad j = a, b, c \quad (10)$$

for eigenvalue $E = V_0(1/\sigma_x + 1/\sigma_y)$ and Gaussian eigenfunction $\phi_{j,\mathbf{v}}(\mathbf{r}, z)$. The eigenvalue E is the same for each sublattice as long as V_0, σ_x and σ_y are identical in all sublattices.

The wave field is decomposed into a sum of the above orbital functions, given by

$$\phi(\mathbf{r}, z) \sim \sum_{\mathbf{v}} [a_{\mathbf{v}}(z) \phi_{a,\mathbf{v}}(\mathbf{r}, z) + b_{\mathbf{v}}(z) \phi_{b,\mathbf{v}}(\mathbf{r}, z) + c_{\mathbf{v}}(z) \phi_{c,\mathbf{v}}(\mathbf{r}, z)] e^{i\mathbf{k} \cdot \mathbf{v} - iEz}, \quad (11)$$

where the orbitals are modulated by the associated coefficients $a_{\mathbf{v}}, b_{\mathbf{v}}, c_{\mathbf{v}}$. We substitute expansion (11) into (7), multiply by $\phi_{i,\mathbf{p}}(\mathbf{r}, z), i = a, b, c$, and integrate over all \mathbf{r} .

The two lattices we consider in detail, Lieb and Kagome, are shown in Figs. 1 and 2, respectively. Both are nondimensionalized so that the distance between nearest neighbors is one. The Lieb lattice sites are separated via the standard basis vectors

$$\mathbf{e}_1 = (1, 0), \quad \mathbf{e}_2 = (0, 1). \quad (12)$$

The Kagome lattice is defined in terms of the vectors

$$\mathbf{v}_1 = \left(\frac{\sqrt{3}}{2}, \frac{1}{2} \right), \quad \mathbf{v}_2 = \left(\frac{\sqrt{3}}{2}, -\frac{1}{2} \right), \quad \mathbf{v}_3 = (0, 1). \quad (13)$$

As a result, the Lieb lattice sites defined in Eq. (2) are given by the sets $\mathcal{R}_a = \{\mathbf{v} : \mathbf{v} = (2\mu + 1)\mathbf{e}_1 + (2\nu)\mathbf{e}_2\}$,

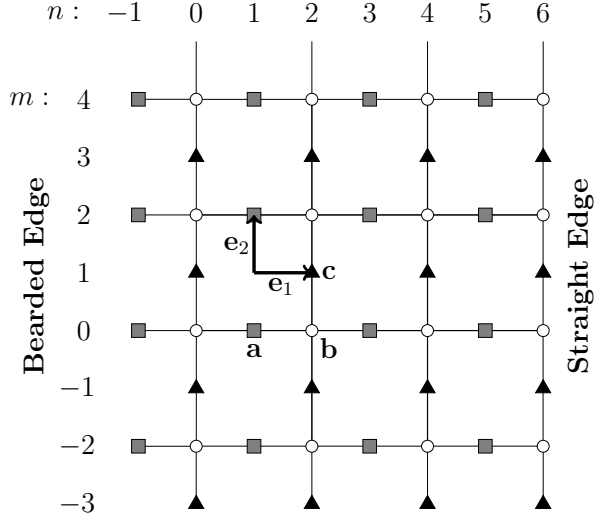


FIG. 1. The Lieb lattice consists of three interpenetrating square sublattices $V_a(\mathbf{r})$ (square site, **a**), $V_b(\mathbf{r})$ (circle site, **b**) and $V_c(\mathbf{r})$ (triangle site, **c**). The lattice vectors \mathbf{e}_1 and \mathbf{e}_2 are defined in (12). Lines denote nearest neighbor interactions.

$\mathcal{R}_b = \{\mathbf{v} : \mathbf{v} = (2\mu)\mathbf{e}_1 + (2\nu)\mathbf{e}_2\}$, $\mathcal{R}_c = \{\mathbf{v} : \mathbf{v} = (2\mu)\mathbf{e}_1 + (2\nu+1)\mathbf{e}_2\}$ for $\mu, \nu \in \mathbb{Z}$. In the case of the Kagome lattice the lattice points are $\mathcal{R}_a = \{\mathbf{v} : \mathbf{v} = (2\mu+1)\mathbf{v}_1 + (2\nu)\mathbf{v}_3\}$, $\mathcal{R}_b = \{\mathbf{v} : \mathbf{v} = (2\mu)\mathbf{v}_1 + (2\nu)\mathbf{v}_2\}$, $\mathcal{R}_c = \{\mathbf{v} : \mathbf{v} = (2\mu+1)\mathbf{v}_2 + (2\nu)\mathbf{v}_3\}$ where $\mu, \nu \in \mathbb{Z}$.

To leading order: in the Lieb lattice the *b* sites interact with both the *a* and *c* sites, whereas the *a*, *c* sites only interact with the *b* sites; in the Kagome lattice all sites interact with each other. For experimental parameters used in [3] the coefficients in Eqs. (14)-(16) and (21)-(23) that represent nearest neighbor interaction are on the order of $\mathcal{O}(10^{-1})$, while the next-nearest neighbor coupling (not included) is on the order of $\mathcal{O}(10^{-3})$ for Lieb and $\mathcal{O}(10^{-5})$ for Kagome. For this reason, we only consider nearest neighbor overlap, but emphasize that longer range interactions could also be taken into account.

A. Lieb Tight-binding Approximation

Here we present a tight-binding model for the Lieb lattice. In deriving this set of equations only the dominant self and nearest neighbor interactions are taken into account. As indicated earlier, since this is a leading order calculation we do not include any direct interaction between the *a* and *c* lattice sites (see Fig. 1) in our derivation. Weak on-site cubic nonlinearity is included in the equations. The semi-discrete system of equations are given by

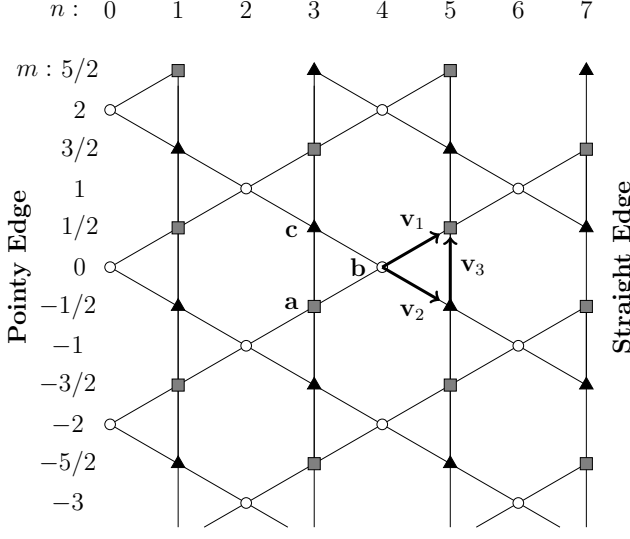


FIG. 2. The Kagome lattice consists of three interpenetrating triangular sublattices $V_a(\mathbf{r})$ (square sites, **a**), $V_b(\mathbf{r})$ (circle sites, **b**) and $V_c(\mathbf{r})$ (triangle sites, **c**). The lattice vectors \mathbf{v}_1 , \mathbf{v}_2 , and \mathbf{v}_3 are given in (13). Lines denote nearest neighbor interactions.

$$i \frac{da_{2m,2n-1}}{dz} + (\Delta \mathbf{h}_{ab} \cdot \mathbf{A}_z + \gamma_{nl} |a_{2m,2n-1}|^2) a_{2m,2n-1} + \sum_{\mathbf{v}=\pm \mathbf{e}_1} \mathbb{L}(\mathbf{v} - \Delta \mathbf{h}_{ab}(z)) b_{2m,(2n-1)\pm 1} = 0, \quad (14)$$

$$i \frac{db_{2m,2n}}{dz} + \gamma_{nl} |b_{2m,2n}|^2 b_{2m,2n} + \sum_{\mathbf{v}=\pm \mathbf{e}_1} \mathbb{L}_+(\mathbf{v} - \Delta \mathbf{h}_{ba}(z)) a_{2m,2n\pm 1} + \sum_{\mathbf{v}=\pm \mathbf{e}_2} \mathbb{L}_+(\mathbf{v} - \Delta \mathbf{h}_{bc}(z)) c_{2m\pm 1,2n} = 0, \quad (15)$$

$$i \frac{dc_{2m+1,2n}}{dz} + (\Delta \mathbf{h}_{cb} \cdot \mathbf{A}_z + \gamma_{nl} |c_{2m+1,2n}|^2) c_{2m+1,2n} + \sum_{\mathbf{v}=\pm \mathbf{e}_2} \mathbb{L}(\mathbf{v} - \Delta \mathbf{h}_{cb}(z)) b_{(2m+1)\pm 1,2n} = 0, \quad (16)$$

such that

$$\sum_{\mathbf{v}=\pm \mathbf{e}_1} \mathbb{L}(\mathbf{v} - \Delta \mathbf{h}_{ab}(z)) b_{2m,(2n-1)\pm 1} \equiv \mathbb{L}(\mathbf{e}_1 - \Delta \mathbf{h}_{ab}(z)) b_{2m,2n} + \mathbb{L}(-\mathbf{e}_1 - \Delta \mathbf{h}_{ab}(z)) b_{2m,(2n-2)},$$

where $\mathbb{L}_+(\mathbf{r}) = \mathbb{L}(\mathbf{r}) + i\mathbb{R}(\mathbf{r})$ and $\gamma_{nl} \geq 0$. The definitions of the coefficients \mathbb{L} , \mathbb{R} and γ_{nl} , in terms of physical parameters, are given in Appendix B. Note that Eq. (15), unlike the other two equations, does not contain a $\Delta \mathbf{h}_{bb} \cdot \mathbf{A}_z$ term since $\Delta \mathbf{h}_{bb} = 0$.

We concentrate on edge modes that propagate in a semi-infinite strip. Outside this lattice region the light beam is assumed to be negligibly small. Hence we take zero boundary conditions on the left and right sides. Along the infinite m -direction we take large computational domains and implement periodic boundary conditions. For the lattice displayed in Fig. 1 we show two possible edge types: “bearded” and “straight.” Among the left and right edges any combination of these two edge types is possible e.g. straight-straight, straight-bearded, or bearded-straight.

We look for edge mode solutions located along the left or right side boundaries of the form

$$\begin{aligned} a_{2m,2n-1}(z) &= a_{2n-1}(z; \omega) e^{i2m\omega}, \\ b_{2m,2n}(z) &= b_{2n}(z; \omega) e^{i2m\omega}, \\ c_{2m+1,2n}(z) &= c_{2n}(z; \omega) e^{i(2m+1)\omega}, \end{aligned} \quad (17)$$

which reduce Eqs. (14)-(16) to

$$\begin{aligned} i \frac{da_{2n-1}}{dz} + (\Delta \mathbf{h}_{ab} \cdot \mathbf{A}_z + \gamma_{nl} |a_{2n-1}|^2) a_{2n-1} \\ + \sum_{\mathbf{v}=\pm \mathbf{e}_1} \mathbb{L}(\mathbf{v} - \Delta \mathbf{h}_{ab}(z)) b_{(2n-1)\pm 1} = 0, \end{aligned} \quad (18)$$

$$\begin{aligned} i \frac{db_{2n}}{dz} + \gamma_{nl} |b_{2n}|^2 b_{2n} \\ + \sum_{\mathbf{v}=\pm \mathbf{e}_1} \mathbb{L}_+(\mathbf{v} - \Delta \mathbf{h}_{ba}(z)) a_{2n\pm 1} \\ + \sum_{\mathbf{v}=\pm \mathbf{e}_2} \mathbb{L}_+(\mathbf{v} - \Delta \mathbf{h}_{bc}(z)) c_{2n} e^{\pm i\omega} = 0, \end{aligned} \quad (19)$$

$$\begin{aligned} i \frac{dc_{2n}}{dz} + (\Delta \mathbf{h}_{cb} \cdot \mathbf{A}_z + \gamma_{nl} |c_{2n}|^2) c_{2n} \\ + \sum_{\mathbf{v}=\pm \mathbf{e}_2} \mathbb{L}(\mathbf{v} - \Delta \mathbf{h}_{cb}(z)) b_{2n} e^{\pm i\omega} = 0. \end{aligned} \quad (20)$$

B. Kagome Tight-binding Approximation

Next we give the tight-binding approximation for the Kagome lattice. As mentioned above, each lattice site interacts with two of the other lattice sites (e.g. b sites interact with nearest a and c sites). Similar to the Lieb case, we study a semi-infinite strip domain: zero boundary conditions on the left and right edges, and periodic boundary conditions along the m -direction. Similar to the Lieb lattice we focus on two types of boundary conditions: “pointy” (the analog of bearded for Lieb) and “straight” (see Fig. 2). Any combination of these two boundary types can be accommodated.

Taking into account self and nearest neighbor interactions and weak on-site nonlinearity we arrive at the following system of equations describing this Floquet lat-

tic

$$\begin{aligned} i \frac{da_{mn}}{dz} + (\Delta \mathbf{h}_{ab} \cdot \mathbf{A}_z + \gamma_{\text{nl}} |a_{mn}|^2) a_{mn} \\ + \sum_{\mathbf{v}=\pm\mathbf{v}_1} \mathbb{L}(\mathbf{v} - \Delta \mathbf{h}_{ab}(z)) b_{m\pm 1/2, n\pm 1} \\ + \sum_{\mathbf{v}=\pm\mathbf{v}_3} \mathbb{L}_+(\mathbf{v} - \Delta \mathbf{h}_{ac}(z)) c_{m\pm 1, n} = 0, \end{aligned} \quad (21)$$

$$\begin{aligned} i \frac{db_{mn}}{dz} + \gamma_{\text{nl}} |b_{mn}|^2 b_{mn} \\ + \sum_{\mathbf{v}=\pm\mathbf{v}_1} \mathbb{L}_+(\mathbf{v} - \Delta \mathbf{h}_{ba}(z)) a_{m\pm 1/2, n\pm 1} \\ + \sum_{\mathbf{v}=\pm\mathbf{v}_2} \mathbb{L}_+(\mathbf{v} - \Delta \mathbf{h}_{bc}(z)) c_{m\mp 1/2, n\pm 1} = 0, \end{aligned} \quad (22)$$

$$\begin{aligned} i \frac{dc_{mn}}{dz} + (\Delta \mathbf{h}_{cb} \cdot \mathbf{A}_z + \gamma_{\text{nl}} |c_{mn}|^2) c_{mn} \\ + \sum_{\mathbf{v}=\pm\mathbf{v}_3} \mathbb{L}_+(\mathbf{v} - \Delta \mathbf{h}_{ca}(z)) a_{m\pm 1, n} \\ + \sum_{\mathbf{v}=\pm\mathbf{v}_2} \mathbb{L}(\mathbf{v} - \Delta \mathbf{h}_{cb}(z)) b_{m\mp 1/2, n\pm 1} = 0, \end{aligned} \quad (23)$$

such that

$$\begin{aligned} \sum_{\mathbf{v}=\pm\mathbf{v}_1} \mathbb{L}(\mathbf{v} - \Delta \mathbf{h}_{ab}(z)) b_{m\pm 1/2, n\pm 1} \equiv \\ \mathbb{L}(\mathbf{v}_1 - \Delta \mathbf{h}_{ab}(z)) b_{m+1/2, n+1} \\ + \mathbb{L}(-\mathbf{v}_1 - \Delta \mathbf{h}_{ab}(z)) b_{m-1/2, n-1}, \end{aligned}$$

where $\mathbb{L}_+(\mathbf{r}) = \mathbb{L}(\mathbf{r}) + i\mathbb{R}(\mathbf{r})$. The coefficients $\mathbb{L}(\mathbf{r})$, $\mathbb{R}(\mathbf{r})$ and γ_{nl} are defined in Appendix B.

We are interested in edge mode solutions of the form

$$\begin{aligned} a_{mn}(z) &= a_n(z; \omega) e^{im\omega}, \\ b_{mn}(z) &= b_n(z; \omega) e^{im\omega}, \\ c_{mn}(z) &= b_n(z; \omega) e^{im\omega}, \end{aligned} \quad (24)$$

for real values of ω which yield

$$\begin{aligned} i \frac{da_n}{dz} + (\Delta \mathbf{h}_{ab} \cdot \mathbf{A}_z + \gamma_{\text{nl}} |a_n|^2) a_n \\ + \sum_{\mathbf{v}=\pm\mathbf{v}_1} \mathbb{L}(\mathbf{v} - \Delta \mathbf{h}_{ab}(z)) e^{\pm i\omega/2} b_{n\pm 1} \\ + \sum_{\mathbf{v}=\pm\mathbf{v}_3} \mathbb{L}_+(\mathbf{v} - \Delta \mathbf{h}_{ac}(z)) e^{\pm i\omega} c_n = 0, \end{aligned} \quad (25)$$

$$\begin{aligned} i \frac{db_n}{dz} + \gamma_{\text{nl}} |b_n|^2 b_n \\ + \sum_{\mathbf{v}=\pm\mathbf{v}_1} \mathbb{L}_+(\mathbf{v} - \Delta \mathbf{h}_{ba}(z)) e^{\pm i\omega/2} a_{n\pm 1} \\ + \sum_{\mathbf{v}=\pm\mathbf{v}_2} \mathbb{L}_+(\mathbf{v} - \Delta \mathbf{h}_{bc}(z)) e^{\mp i\omega/2} c_{n\pm 1} = 0, \end{aligned} \quad (26)$$

$$\begin{aligned} i \frac{dc_n}{dz} + (\Delta \mathbf{h}_{cb} \cdot \mathbf{A}_z + \gamma_{\text{nl}} |c_n|^2) c_n \\ + \sum_{\mathbf{v}=\pm\mathbf{v}_3} \mathbb{L}_+(\mathbf{v} - \Delta \mathbf{h}_{ca}(z)) e^{\pm i\omega} a_n \\ + \sum_{\mathbf{v}=\pm\mathbf{v}_2} \mathbb{L}(\mathbf{v} - \Delta \mathbf{h}_{cb}(z)) e^{\mp i\omega/2} b_{n\pm 1} = 0. \end{aligned} \quad (27)$$

III. LINEAR FLOQUET BANDS AND EDGE STATE DYNAMICS

We now compute the linear ($\gamma_{\text{nl}} = 0$) Floquet bands for the tight-binding systems described above. To accomplish this we evolve the reduced systems (18)-(20) or (25)-(27) one period in z using an identity initial condition. From this we obtain the monodromy matrix at $z = T$ (where T is the helix pitch or period: $T = 2\pi/\Omega$). The eigenvalues of the monodromy matrix are the Floquet (characteristic) multipliers $\lambda(\omega)$. The Floquet exponents are computed, up to an additive constant, by

$$\alpha(\omega) = \frac{i \ln[\lambda(\omega)]}{T} + \frac{2\pi l}{T}, \quad l \in \mathbb{Z}. \quad (28)$$

Since the range of possible lattice rotation patterns is very large we focus our attention on driving patterns which have been shown to demonstrate interesting band structures in other lattice systems. Previous examples include same rotation in honeycomb lattices [3], or π -phase offset among the sublattices that generate Weyl type-II points [7]. In particular we concentrate on the following driving patterns:

- same (in-phase) rotation

$$\mathbf{h}_j(z) = \eta (\cos(\Omega z), \sin(\Omega z)), \quad (29)$$

- different radii, in-phase

$$\mathbf{h}_j(z) = R_j \eta (\cos(\Omega z), \sin(\Omega z)), \quad R_j \leq 1 \quad (30)$$

- π -phase offset

$$\mathbf{h}_j(z) = \eta (\cos(\Omega z + \chi_j), \sin(\Omega z + \chi_j)), \quad \chi_j = 0, \pi \quad (31)$$

- counter rotation

$$\mathbf{h}_j(z) = \eta (\cos(r_j \Omega z), \sin(r_j \Omega z)), \quad r_j = \pm 1 \quad (32)$$

- different frequency

$$\mathbf{h}_j(z) = \eta (\cos(l_j \Omega z), \sin(l_j \Omega z)), \quad l_j \in \mathbb{N}, \quad (33)$$

- quasi one-dimensional motion

$$\begin{aligned} \mathbf{h}_j(z) &= \eta (p_j \cos(\Omega z), q_j \sin(\Omega z)), \\ p_j, q_j &= 0, 1, \quad p_j + q_j = 1, \end{aligned} \quad (34)$$

where $j = a, b, c$. We point out that each of the driving functions above have period T i.e. $\mathbf{h}_j(z + T) = \mathbf{h}_j(z)$, where $T = 2\pi/\Omega$.

For all examples considered in this paper we use lattice depth $V_0^2 = 45$ and angular frequency $\Omega = 2\pi/1.5$; this corresponds a helix pitch of $T = 1.5$. These parameters are taken to model the experimental parameters reported in [3].

A. Lieb Floquet bands

In this section we compute the Floquet bands for the Lieb lattice. These bands, defined in Eq. (28), are calculated for the linear ($\gamma_{nl} = 0$) system of equations given in Eqs. (18)-(20). The band structures consist of bulk or extended modes (indicated by solid black regions) and edge or localized modes (indicated by curves, highlighted in color). We show only the real part of α as the imaginary (unstable) part is typically very small.

In the absence of helical driving ($\eta = 0$) the Lieb dispersion bands are known to possess a flat band that spans the Brillouin zone cf. [19]. Regardless of the left/right boundary conditions (e.g. bearded/bearded, bearded/straight, or straight/straight) the band diagram resembles that shown in Fig. 3. Flat (stationary) edges modes are found to exist along both edges.

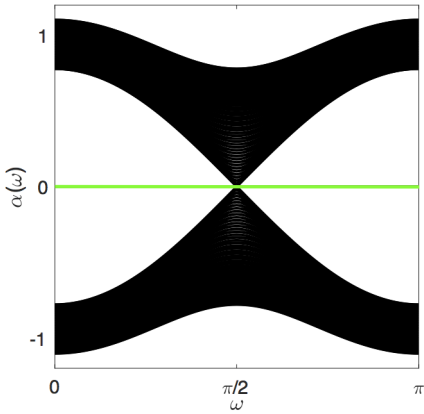


FIG. 3. (Color online) Lieb Floquet bands with no lattice driving. Green curve indicates that flat band modes are located on both edges. The parameters used are: $\eta = 0$, $\sigma_x = \sigma_y = 0.3$.

The first driven case considered is that of same rotation (29) among the waveguides. Several typical Floquet bands are shown in Fig. 4 for different boundary condition combinations. Each case contains traveling ($\alpha'(\omega) \neq 0$) and stationary ($\alpha'(\omega) = 0$) modes; one of each type on both edges (left and right). Moreover each boundary type is found to exhibit a distinct signature in its band structure. For instance, the Floquet bands on the straight edge possess a steep slope (large group velocity), particularly near $\omega = \pi/2$, whereas the bearded edge modes have a shallow slope (smaller group velocity)

throughout the Brillouin zone. As a consequence, for this rotation pattern there are fast edges (straight) and slow edges (bearded).

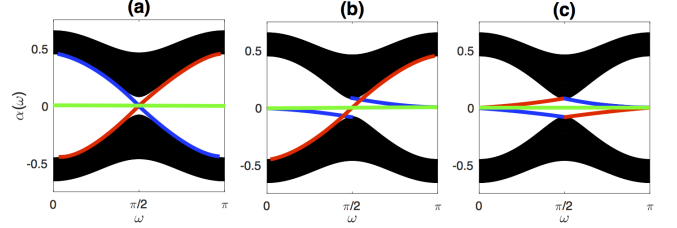


FIG. 4. (Color online) Lieb Floquet bands for same phase lattice rotation (29) with different boundary conditions. The boundary condition on the left [right] edge is: (a) straight [straight], (b) bearded [straight], and (c) bearded [bearded]. Red curves indicate edge modes on right edge, blue curves denote left edge modes, and the green curves designate flat band modes on both edges. The parameters used are: $\eta = 2/3$, $\sigma_x = \sigma_y = 0.3$.

For all remaining band calculations we use the boundary combination shown in Fig. 1, namely bearded on the left edge and straight on the right. The next case considered is that of π -offset rotation (31) with $\chi_a = \chi_c = \pi$ and $\chi_b = 0$. The corresponding Floquet bands are displayed in Fig. 5 for three different values of η i.e. radius. Each case contains a set of topologically protected edge states residing in the central gaps. One significant difference between these bands and those found in Fig. 4(b) is the absence of any flat band modes. In addition, at a certain radius threshold [see Fig. 5(b)] the gap between different branches of the Floquet exponent (28) closes. In terms of the band structure, this means the bulk bands in Fig. 5(b) touch near the Floquet edge $\alpha_{\text{edge}} = \pm\pi/T \approx \pm 2.1$. Increasing the helix radius beyond this threshold spawns an entirely new family of edge states located near the Floquet edge. The phase offset rotation pattern has been shown to generate similar band bifurcation patterns in honeycomb and square lattices [4–6]; we will also see this later in Kagome lattices. Finally, we point out that the bearded edge modes shown in Fig. 5 move considerably faster than those in Fig. 4(b). Hence it is possible, (by changing the lattice rotation pattern) to support faster edge mode propagation along a bearded edge.

Many other lattice rotation patterns are also found to support localized edge states. In Fig. 6 we show Floquet bands for various driving patterns on the Lieb lattice. The dispersion curves corresponding to same rotation (29) among elliptical ($\sigma_x \neq \sigma_y$), rather than circular, waveguides are shown in Figs. 6(a) and 6(b). In the former case ($\sigma_x < \sigma_y$) the major axis of the ellipse is parallel to the m -direction, while in the latter scenario ($\sigma_x > \sigma_y$) the major axis is parallel to the n -direction. Doing this is found to either squeeze [see Fig. 6(a)] or stretch [see Fig. 6(b)] the width of the bulk bands. In the former case the slope of the straight (right) edge modes increase, while in the latter case the modes slow down. We find that this lattice rotation arrangement does support flat

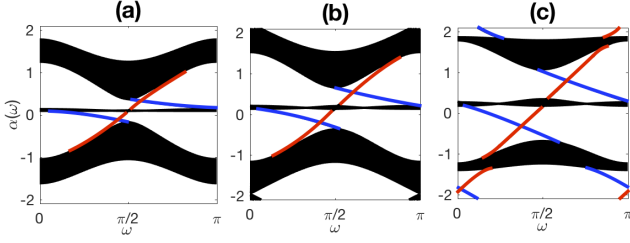


FIG. 5. (Color online) Lieb Floquet bands for π -offset rotation (31) where $\chi_a = \chi_c = \pi, \chi_b = 0$. The boundary condition on the left [right] edge is bearded [straight]. Red curves indicate edge modes on right edge, blue curves denote left edge modes. The parameters used are: (a) $\eta = 1.4/15$, (b) $\eta = 1.8/15$, and (c) $\eta = 2.2/15$ with $\chi_a = \chi_c = \pi, \chi_b = 0, \sigma_x = \sigma_y = 0.3$.

band modes on either edge.

Next we consider when the sublattices are rotating in-phase with each other, but with different radii (30) where $R_a = R_c = 0.6, R_b = 1$. Examining the corresponding band structure in Fig. 6(c) we observe the presence of unidirectional modes and the absence of any flat band states. The next set of bands correspond to different frequency (33) among the sublattices. In particular we examine when the a and c lattice sites rotate at twice the frequency of the b sites i.e. $l_a = l_c = 2, l_b = 1$. Overall, the band structure resembles the same rotation case shown in Fig. 4(b) without, however, the presence of any flat band modes. We point out that in this case the imaginary part of the Floquet exponent is $\mathcal{O}(10^{-4})$ near the point $\omega = 1.4$ and could indicate a weak instability. The bands corresponding to counter rotation (32) are shown in Fig. 6(e) for the parameters $r_a = r_c = -1$ and $r_b = 1$. This means that the b sites are rotating in a counter-clockwise fashion while the a and c sites move in the clockwise direction. No localized modes are found in this case for parameters similar to those presented in Fig. 6(e).

The final case is that of quasi one-dimensional motion (34) where each sublattice moves in only one direction. We consider a scenario in which the a and c sites oscillate only in the m -direction ($p_a = p_c = 0, q_a = q_c = 1$), while the b sites oscillate only in the n -direction ($p_b = 1, q_b = 0$). The corresponding bands are shown in Fig. 6(f). For this relatively simple lattice motion we identify the presence unidirectional traveling edge modes. Looking closer we note that these modes travel in an orientation opposite those found in previous cases. In contrast to the previous cases, straight (right) edge modes move in the negative direction ($\alpha'(\omega) < 0$), while pointy (left) edge modes travel in the positive direction ($\alpha'(\omega) > 0$). No flat band modes are found.

In summary, Lieb lattices with different driving provide a remarkably large variety of indicated topologically protected edge modes: as described by the red-blue colors of the unidirectional modes in Figs. 4, 5, and Fig. 6 all except (e).

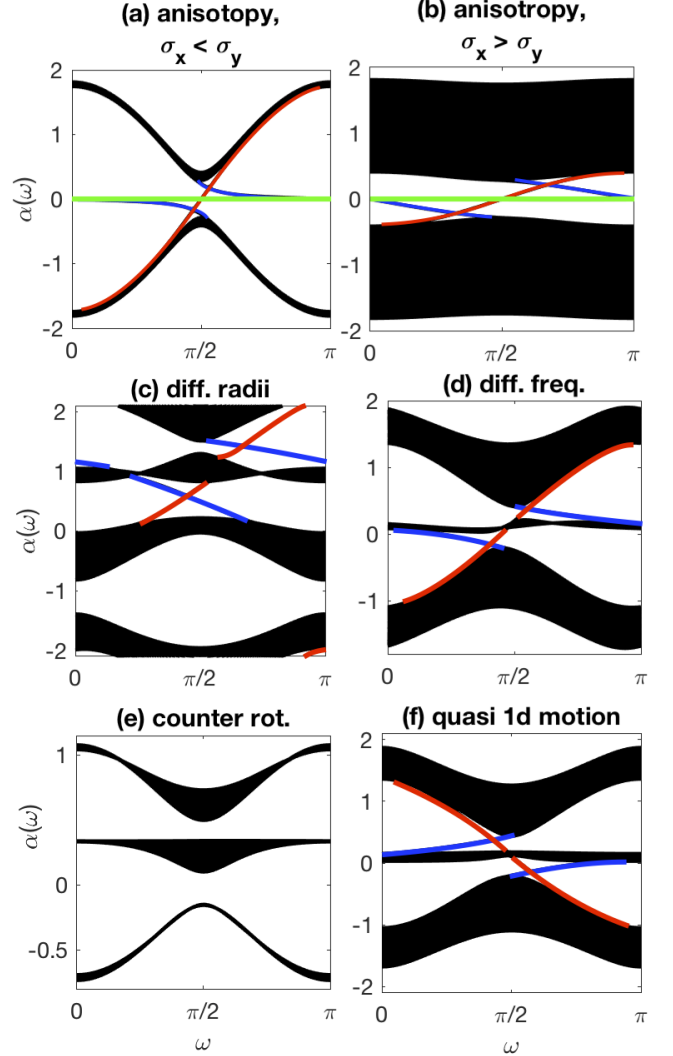


FIG. 6. (Color online) Lieb Floquet bands for various rotation patterns. The boundary condition on the left [right] edge is bearded [straight]. Red curves indicate edge modes on right edge, blue curves denote left edge modes, and the green curves designate flat band modes on both edges. The parameters used are: (a-b) $\eta = 2/3, \sigma_x = 0.3, \sigma_y = 0.5$ and (b) $\sigma_x = 0.5, \sigma_y = 0.3$; (c) $\eta = 2/3, R_a = R_c = 3/5, R_b = 1$, (d) $\eta = 2.2/15, l_a = l_c = 2, l_b = 1$, (e) $\eta = 3/15, r_a = r_c = -1, r_b = 1$, (f) $\eta = 3/15, p_a = p_c = 0, p_b = 1$; with $\sigma_x = \sigma_y = 0.3$ in all except (a) $\sigma_x = 0.3, \sigma_y = 0.5$ and (b) $\sigma_x = 0.5, \sigma_y = 0.3$.

B. Lieb edge mode dynamics

In this section we present mode evolutions for the edge states found above. Specifically, we integrate the full Lieb tight-binding system (14)-(16) for an edge mode with a localized envelope in m . The initial conditions taken are

$$\begin{aligned} a_{2m,2n-1}(0) &= \operatorname{sech}(2m\mu) a_{2n-1}(\omega) e^{i2m\omega}, \\ b_{2m,2n}(0) &= \operatorname{sech}(2m\mu) b_{2n}(\omega) e^{i2m\omega}, \\ c_{2m+1,2n}(0) &= \operatorname{sech}((2m+1)\mu) c_{2n}(\omega) e^{i(2m+1)\omega}, \end{aligned} \quad (35)$$

using a typical value $\mu = 0.1$. The edge eigenmodes $a_{2n-1}(\omega), b_{2n}(\omega)$, and $c_{2n}(\omega)$ are obtained directly from solving system (18)-(20) at a chosen ω . In all cases the eigenmode two-norm is fixed to one i.e. $\sum_n (|a_{2n-1}|^2 + |b_{2n}|^2 + |c_{2n}|^2) = 1$. We take periodic boundary conditions in m (top/bottom edges) and bearded-straight zero boundary conditions in n . The left-most lattice site is located at $n = -1$, while the right-most site is $n = N$, where N is taken to be large $\sim O(100)$. The system is integrated using a fourth-order Runge-Kutta method.

The z -dynamics for several edge mode profiles are shown in Fig. 7. For simplicity of presentation, we only show the most dominant (largest magnitude) sublattice mode. The evolutions shown in Figs. 7(a-d) correspond to same rotation among the three sublattices, the Floquet bands of which are shown in Fig. 4(b). The two traveling modes ($\alpha'(\omega) \neq 0$) are observed to propagate with constant velocity in either the negative (on the left side) [see Fig. 7(a)] or positive (on the right side) direction [see Fig. 7(b)]. As expected, the mode on the bearded edge travels considerably slower than the straight edge mode. In order to get a well localized mode the value of ω must be chosen well-separated from the bulk bands. This is why the same rotation mode shown in Fig. 7(a) has a different frequency than the others. When an edge mode with a corresponding Floquet exponent located near a bulk band is used the mode is found to *not* maintain its well-localized structure over long distances and to *not* propagate through lattice defects. This is discussed in Sec. IV.

Next we evolve the stationary flat band states in Fig. 4(b). When solving for the Floquet exponent on the straight edge the algorithm we use produces two stationary modes; one with $|\alpha(1.65)| = O(10^{-4})$ and another at $|\alpha(1.65)| = O(10^{-11})$. In Fig. 7 we only consider the mode whose magnitude is smaller. We note that the magnitude of these flat band modes is found to peak not along the boundary, but instead at an interior column (at $n = 0$ on the left or $n = N - 1$ on the right). The flat band evolutions are shown in Figs. 7(c-d). As expected, these modes do not move from their initial position.

Interestingly, these flat band modes do not appear to suffer from diffraction. To highlight this we evolve the same rotation modes shown in Figs. 7(a-d) over very long distances (up to $z = 1000$). In the course of integration we monitor the maximum magnitude

$$M = \max_{m,n} |f_{mn}|, \quad (36)$$

and the participation number

$$P = \frac{\left(\sum_{m,n} |f_{mn}|^2\right)^2}{\sum_{m,n} |f_{mn}|^4}, \quad (37)$$

of the sublattice modes shown in Fig. 7 (so either $f = a$ or $f = c$). The results are presented in Fig. 8. In Fig. 8(a) we see that, unlike the traveling modes, over long distances the non-dispersive ($\alpha''(\omega) = 0$) flat band modes

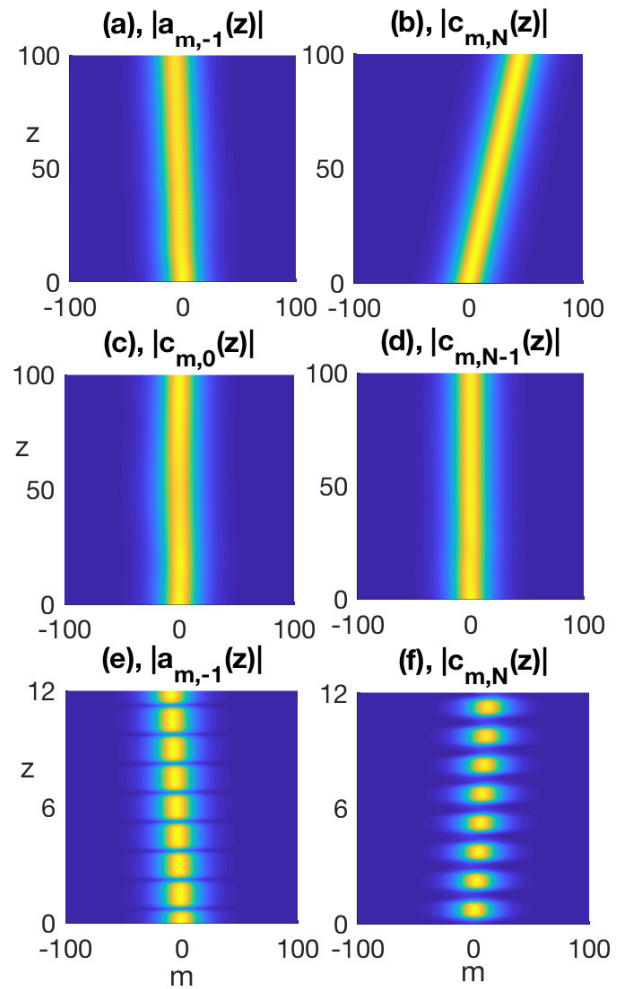


FIG. 7. Evolution of edge profile in the Lieb lattice. The edge modes shown in panels (a-d) correspond to the Floquet bands in Fig. 4(b) at: (a) $(\omega, \alpha) = (1.8, 0.0628)$, (b) $(1.65, 0.0362)$, (c-d) $(1.65, 0)$. The edge states in panels (e-f) correspond to the bands shown in Fig. 5(c) at $(\omega, \alpha) = (e) (.2, -1.97)$ and $(f) (.2, -1.69)$.

maintain their peak amplitude after a short transient period. Moreover the participation number (which gives an indication of the mode width) shows that flat band modes are not diffracting or spreading at all over very long distances, unlike the traveling modes. It has been suggested the flat band modes could serve as good transmitters of optical information [24].

The final set of evolutions we present is that of π -offset rotation. We omit the edge mode dynamics for the bands shown in Fig. 6, but note that many similar evolution patterns are observed in those cases. We focus on the π -offset modes near the Floquet edge in Fig. 5(c). The corresponding mode evolutions are displayed in Fig. 7(e-f). The mode profiles on both sides are observed to oscillate with the same period as the lattice driving ($T = 1.5$). Moreover along the bearded edge [see Fig. 7(e)] energy fluctuates back-and-forth between the

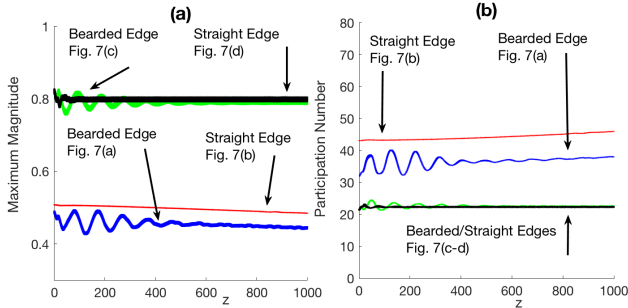


FIG. 8. (a) Maximum magnitude (36) and (b) participation number (37) evolutions for the modes shown in Figs. 7(a-d).

a/c sites (in-phase with each other) and the *b*-sites (out-of-phase). In Fig. 7(f) the straight edge mode shown, $c_{m,N}$, has a similar, but out-of-phase, evolution pattern with the *b*-sites; meanwhile the *a* lattice modes are relatively small in comparison.

C. Kagome Floquet bands

In this section we compute Floquet bands for the Kagome lattice. The dispersion curves are computed in the same way as the Lieb bands in the previous section, via the Floquet exponents (28), for the rotation patterns listed in Eqs. (29)-(34). All bands are computed from the one-dimensional tight-binding system given in Eqs. (25)-(27).

Before considering the driven case we first examine the dispersion bands without any longitudinal driving ($\eta = 0$). The Floquet bands for different boundary conditions are displayed in Fig. 9, where both traveling and non-traveling edge states are observed. Regardless of the edge type we find a flat band. By introducing a pointy edge (see Fig. 2) we observe a “vine” type family of modes which does not span a band gap. To our knowledge flat band modes have not previously been considered in the context of a kagome photonic lattice waveguide. Interestingly, below we do not find any flat bands like these in the presence of periodic driving (unlike the Lieb lattice above).

The first driven case to consider is that of same rotation among all sublattices (29). The corresponding band diagrams are shown in Fig. 10 for three different boundary condition combinations. Similar to the Lieb lattice above, here we observe that the different boundary conditions carry distinguishable band structure. Both edge types possess a traveling edge mode in the central gap ($\alpha(\omega) \leq 0$). These unidirectional edge modes cross from an upper bulk band to a lower bulk band and have sign-definite group velocity throughout the gap; they are expected to be topologically protected. Additionally, for the straight edge there are edge modes near $\alpha = 0.5$ that are nearly flat. On the other hand, when a pointy edge is introduced we observe the “vine” type curve in the upper gap ($0.3 \leq \alpha(\omega) \leq 0.4$). We point out that the

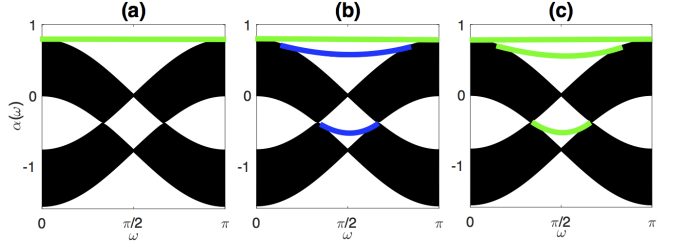


FIG. 9. (Color online) Kagome Floquet bands in the absence of rotation with different boundary conditions. The boundary condition on the left [right] edge is: (a) straight [straight], (b) pointy [straight], and (c) pointy [pointy]. Blue curves denote left edge modes and the green curves designate flat band modes on both edges. The parameters used are: $\eta = 0$, $\sigma_x = \sigma_y = 0.3$.

pointy “vine” edge curves are not slope-definite i.e. depending on ω , the group velocity may be either positive ($\alpha'(\omega) > 0$) or negative ($\alpha'(\omega) < 0$); hence these modes will not be topologically protected (cf. Fig. 15). Moreover, the pointy edge (blue) mode in the upper gap actually spans the gap, unlike the pointy mode in the upper gap considered in the absence of driving in Fig. 9(b).

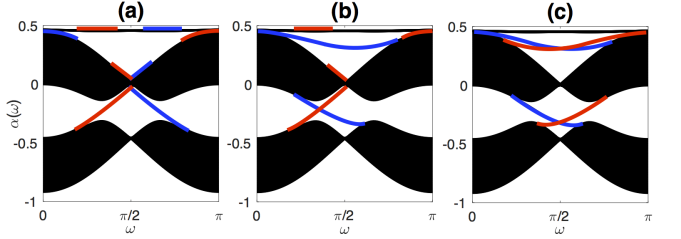


FIG. 10. (Color online) Kagome Floquet bands for same phase lattice rotation (29) with different boundary conditions. The boundary condition on the left [right] edge is: (a) straight [straight], (b) pointy [straight], and (c) pointy [pointy]. Red curves indicate edge modes on right edge, blue curves denote left edge modes. The parameters used are: $\eta = 2/3$, $\sigma_x = \sigma_y = 0.3$.

For the remaining Kagome band diagrams we consider pointy-straight boundary conditions, similar to those in Fig. 2. When the individual waveguides are elliptical in shape (major axis parallel to the *n*-direction, $\sigma_x > \sigma_y$) and all sublattices are rotating in-phase with each other (29), we find the band diagram shown in Fig. 11(a). This band structure bears little resemblance to the isotropic bands found in Fig. 10(b). The pointy edge bands are observed to have slopes of positive or negative sign suggesting the absence of unidirectional propagation. We also note the presence of edge states located near $(\omega, \alpha) = (\pi/2, \pm 1)$ located on the straight edge. Additionally, there is a set of topological modes located on the straight edge that span the central gaps.

We next examine different radii among the sublattices (30). In particular we consider when the *a* and *c* sublattices have smaller radii ($R_a = R_c = 0.6$) than the *b* lattice sites ($R_b = 1$). The corresponding band

diagram is shown in Fig. 11(b). Numerous modes on both edges are found. All modes on the pointy edge appear to be topologically protected and will travel in only one direction. One unusual family of edge states are those on the straight edge which have sign-indefinite group velocity, yet still span the gap [see minimum point near $(\omega, \alpha) = (1.7, 1.4)$]. Unsurprisingly, when one of these modes was propagated into a defect barrier it did backscatter.

The Floquet bands corresponding to different frequency among the sublattices (33) are shown in Fig. 11(c). Here we take the a and c sublattices to oscillate twice as fast as the b sites i.e. $l_a = l_c = 2, l_b = 1$. In the lower gap modes that travel in either the positive or negative direction are found for both edge types, even though they span the gap. In the upper gap the Floquet bands instead show a topologically protected structure that is not well-separated from the bulk band. We do not call the pointy edge band in the upper gap flat, since it has a small, but nonzero slope.

When a π -phase offset (31) is introduced between the sublattices ($\chi_a = \chi_c = \pi, \chi_b = 0$) a threshold phenomena, similar to that observed in Fig. 5 for the Lieb lattice, is found to occur. Increasing the lattice driving (helix radii) we observe the gap between adjacent Floquet exponent bands (28) to close at some threshold value $\eta_T > 0$ and then reopen with a new family of edge states for $\eta > \eta_T$. In Fig. 11(d) we show the bands above this threshold. The entire Brillouin zone in α , from $[-\pi/T, \pi/T]$, consists of either bulk or edge modes. Numerous unidirectional modes on both edges are found. One non-topological band is noted with an inflection point located nearby $\alpha(1.18) = 0.75$.

Counter rotation among the sublattices (32), specifically when the a and c lattice sites have the opposite orientation to that of the b sites ($r_a = r_c = -1, r_b = 1$), is considered next. The corresponding bands are shown in 11(e). In contrast to the Lieb lattice above [see Fig. 6(e)], here we *do* find some edge mode waves. The pointy (left) edge mode in the lower gap does appear to be bi-directional; this is in contrast with the straight edge mode which are unidirectional and topologically protected. Both Floquet bands in the upper gap have slope that is sign-definite.

The final scenario we investigate is that of the quasi one-dimensional rotation pattern (34). A band diagram for this arrangement is shown in Fig. 11(f). The a and c lattice sites only move in the m -direction ($p_a = p_c = 0$), while the b sites only move in the n -direction ($q_b = 0$). Relative to several previous cases, these edge modes tend to move in a clockwise (as opposed to counter-clockwise) fashion. Among the pointy edge bands, the group velocity of the lower gap curve is found to change sign near $\omega = \pi/2$. With the exception of the small Floquet band located in the very top gap, the modes along the straight edge all appear to be topologically protected modes that travel in one direction.

We point out that the bands shown in Figs. 11(b)–(f) exhibit some small, but non-negligible, imaginary

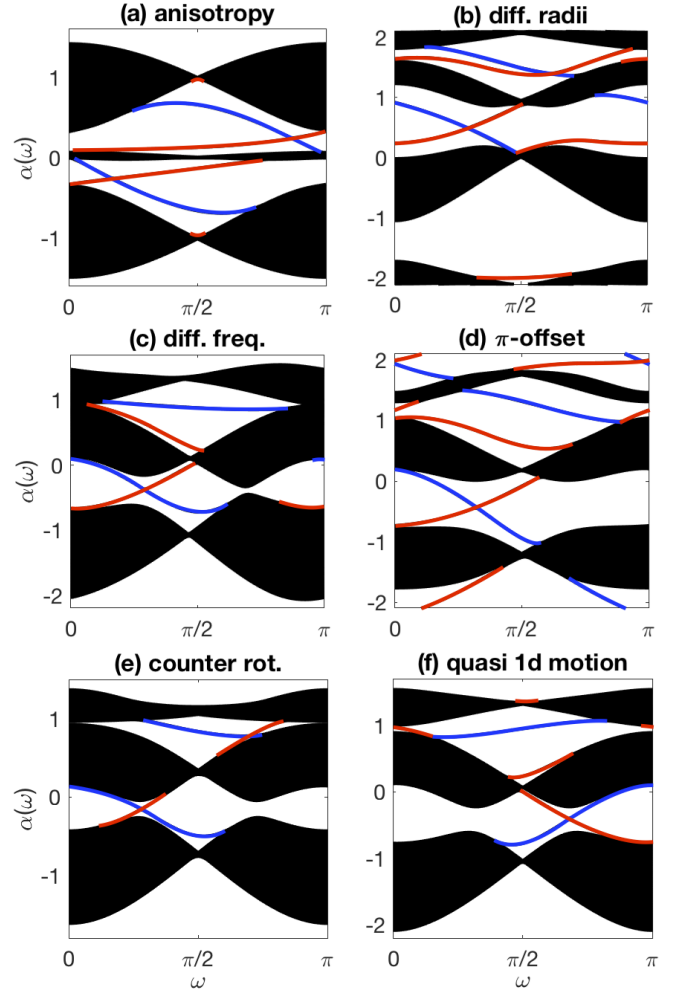


FIG. 11. (Color online) Kagome Floquet bands for various rotation patterns. The boundary conditions on the left [right] edge is pointy [straight]. Red curves indicate edge modes on right edge, blue curves denote left edge modes. The parameters used are: (a) $\eta = 2/3$, (b) $\eta = 2.2/15, R_a = R_c = 3/5, R_b = 1$, (c) $\eta = 2.2/15, l_a = l_c = 2, l_b = 1$, (d) $\eta = 2.2/15, \chi_a = \chi_c = \pi, \chi_b = 0$, (e) $\eta = 1/5, r_a = r_c = -1, r_b = 1$, (f) $\eta = 1/5, p_a = p_c = 0, p_b = 1; \sigma_x = \sigma_y = 0.3$ in all except (a) where $\sigma_x = 0.5, \sigma_y = 0.2$.

(unstable) parts near $\omega = \pi/2$. The magnitude is $|\text{Im } \alpha| = O(10^{-3}) - O(10^{-4})$ or smaller and so this would be unlikely to see any serious effects on the length scales considered here. When these unstable modes do occur they are found only in the extended bulk modes and *not* in the localized edge modes.

It is worth emphasizing the similarities between the Lieb and Kagome lattices. Unidirectionally moving edge states are found for same sublattice rotation (29). Introducing a π -offset (31) among the sublattices introduces a threshold point in η where adjacent Floquet bands touch (see Fig. 5). The quasi one-dimensional rotation pattern (11) is found to reverse the direction modes propagate. To further highlight these commonalities among similar rotation patterns, in Appendix A we have included the Floquet bands for the honeycomb (see Fig. 17) and stag-

gered square (see Fig. 18) lattices for rotation patterns and parameters similar those considered above. Their bands are found to exhibit similar structure in response to similar driving patterns.

D. Kagome edge mode dynamics

In this section we provide evolution dynamics for Kagome edge modes found in the previous section. We integrate Eqs. (21)-(23) using the initial conditions

$$\begin{aligned} a_{mn}(0) &= \operatorname{sech}(\mu m) a_n(\omega) e^{im\omega}, \\ b_{mn}(0) &= \operatorname{sech}(\mu m) b_n(\omega) e^{im\omega}, \\ c_{mn}(0) &= \operatorname{sech}(\mu m) c_n(\omega) e^{im\omega}, \end{aligned} \quad (38)$$

for the edge modes a_n, b_n, c_n found by numerically solving system (25)-(27) at a particular ω . As with the Lieb lattice, we fix $\sum_n (|a_n|^2 + |b_n|^2 + |c_n|^2) = 1$. A slowly-varying sech envelope is attached in the m -direction with $\mu = 0.1$. Here we only show the most dominant sublattice edge mode profile either on the left (pointy edge) at $n = 0$, or the right (straight edge) at $n = N \gg 1$.

Some evolution patterns are shown in Fig. 12. The first case considered is that of same rotation among all sublattices (29) with corresponding Floquet bands shown in Fig. 10(b). At frequency $\omega = 1.2$ each edge has multiple traveling states, each of which propagates with constant velocity. By attaching a slowly-varying envelope along the edge initially (38) we typically excite just the desired mode. When the envelope is too narrow we can excite multiple modes. The evolutions in Figs. 12(a) and (c) are both located along the pointy edge and evolve at a constant negative velocity. The majority of the energy resides in the outermost column of lattice sites, located at $n = 0$ (see Fig. 2), hence we display the b -mode profiles. Along the straight edge there are modes that propagate in either the positive [see Fig. 12(b)] or negative [see Fig. 12(d)] directions. For these modes located on the straight edge [see Figs. 12(b) and (d)] most of the energy is shared by the a and c sites, so we show the c -sublattice mode dynamics.

The evolution of a Kagome lattice with a π -phase offset between the b sites and the a, c lattice sites (31) is shown in Figs. 12(e-f). The corresponding dispersion curves are displayed in Fig. 11(d). The evolution dynamics here resemble those of the Lieb lattice [see Fig. 7(e-f)], as well as those seen in honeycomb and staggered square [4] when the sublattices are out of phase with each other. In both cases shown here, the modes are found to oscillate back-and-forth between the a/c and b lattice sites over the course of one lattice period ($T = 1.5$) and propagate with the group velocity.

IV. DEFECT BARRIER

Edge states associated with other [2-4] helically driven photonic lattices have been shown to exhibit robust unidirectional motion in the presence of lattice defects. Here

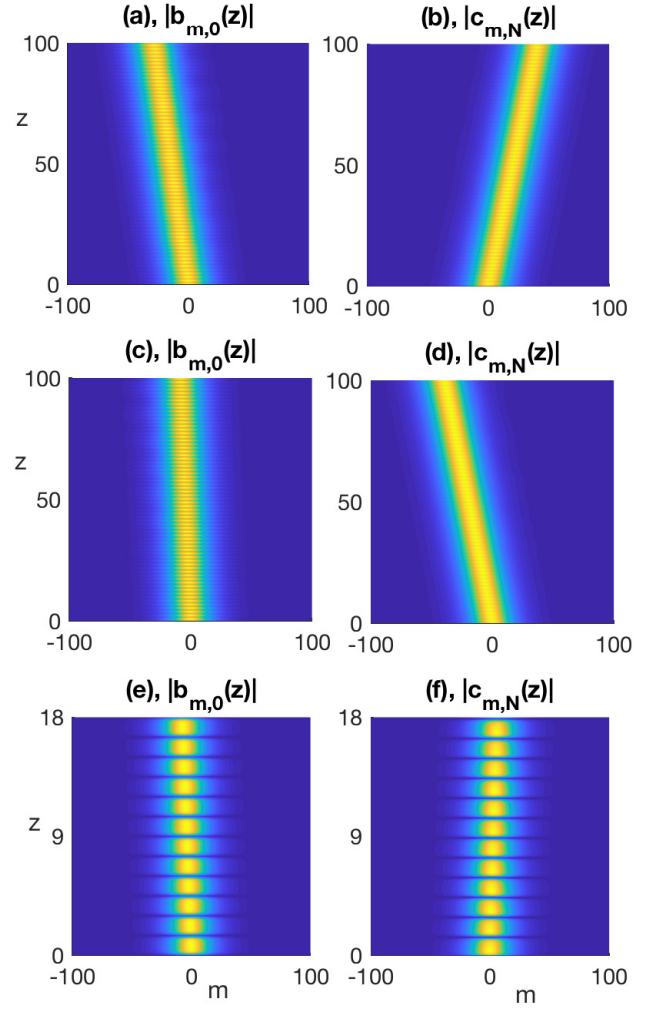


FIG. 12. Evolution of edge profile in the Kagome lattice. The edge modes shown in panels (a-d) correspond to the Floquet bands in Fig. 10(b) at $\omega = 1.2$ with Floquet exponent: $\alpha =$ (a) -0.231 , (b) -0.178 , (c) 0.343 , (d) 0.169 . The edge states in panels (e-f) correspond to the bands shown in Fig. 11(d) at $\omega = 0.2$ where $\alpha =$ (e) 1.84 and (f) 2.04 .

we introduce a lattice defect barrier and monitor the mode evolution as it encounters this barrier. Physically, the defects we consider correspond to the absence of lattice site waveguides. As such, there is little beam propagation in these areas and so we model the beam field to be zero there.

A. Linear Evolution

First, consider the linear Lieb lattice with same rotation waveguide motion; the Floquet bands of which are shown in Fig. 4(b). We evolve an edge state along the straight lattice edge into a defect barrier. In the absence of the barrier, the mode profile evolution is shown in Fig. 7(b). Several snapshots of a topologically protected mode are displayed in the right column of Fig. 13.

All intensities shown here and below are taken relative to the incoming intensity. The topologically protected mode encounters the lattice defect and, instead of scattering backward, it propagates around the barrier. We note that in several of our simulations if the mode envelope in m is taken to be too narrow i.e. μ not small, then noticeable deterioration of the mode can occur due to dispersion.

An example of a Lieb mode evolving through a defect along a bearded edge is shown in the left column of Fig. 13. The rotation pattern used is that of π -offset among the sublattices (31) whose corresponding band diagram is given in Fig. 5(c). The reason we choose to show a mode with this rotation pattern, and not same rotation, is because the group velocity is much larger [cf. Fig. 4(b)], and we do not have to wait as long for the mode to reach the defect. Here the edge state is found to also pass unidirectionally through the defect. This unidirectional propagation is anticipated since the corresponding Floquet band in Fig. 5(c) has sign-definite group velocity along the bearded edge.

We now point out an interesting mode-defect interaction in the case of same sublattice rotation (29) when the Floquet exponent [see Fig. 4(b)] is not well separated from the bulk bands. The evolution of a mode along the straight edge corresponding to a Floquet exponent deep within the band gap was displayed in Fig. 13 (right column). When we instead consider a mode on the same Floquet band, but closer to the bulk bands, we observe significant deterioration of the edge state. In Fig. 14 a mode whose value $\alpha(\omega)$ lies nearby the bulk modes is observed to significantly backscatter away from the defect barrier and diminish in intensity. This mode appears to experience some transfer/leakage of energy into extended bulk states. Topologically protected modes whose Floquet exponent deep in the gap (well away from the bulk) appear to avoid this interaction with the bulk modes.

Next we consider mode evolution for the Kagome lattice in the presence of a defect barrier. Two intriguing cases are presented. The first is that of an edge mode propagating along a straight edge, the band diagram of which is shown in Fig. 10(b). In the absence of a barrier the mode propagation is displayed in Fig. 12(b). The mode evolution with defect is presented in the right column of Fig. 15. The topologically protected edge state works its way around the defect and continues along its way. Since the Floquet band corresponding to this mode is unidirectional i.e. $\alpha'(\omega) > 0$, such one-way motion is expected from a topologically protected mode.

The next case we examine has an edge mode with corresponding dispersion curve that is *not* unidirectional throughout the Brillouin zone, yet still crosses a band gap; i.e. one which is not topologically protected. Consider the pointy edge mode located at $(\omega, \alpha) = (1.2, 0.343)$ in Fig. 10(b). This band has two different slope velocities signs, depending on ω . In the absence of defect, the mode propagation is presented in Fig. 12(c) i.e. propagation with constant negative velocity. With defect, the mode evolution is shown in the left column of

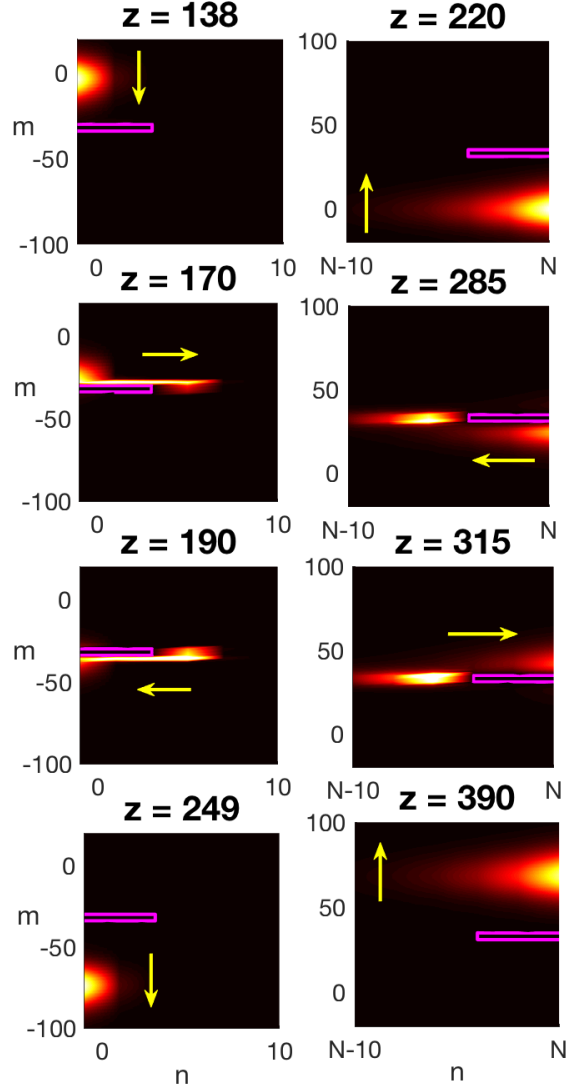


FIG. 13. Linear edge mode dynamics encountering a defect barrier in the Lieb lattice. (Left column) Intensity evolution $|a_{mn}(z)|^2$ along bearded edge with π -offset rotation corresponding to the Floquet bands in Fig. 5(c) with $\omega = 0.2$. (Right column) Intensity evolution $|c_{mn}(z)|^2$ along straight edge for same rotation corresponding to the Floquet bands in Fig. 4(b) with $\omega = 1.65$.

Fig. 15. Here the mode travels towards the barrier, but instead of passing around the defect barrier, it ceases movement in the negative direction and scatters backward with a noticeable loss in intensity. Similar defect dynamics have been observed in honeycomb lattices when the Floquet band slope is not sign-definite [4].

B. Nonlinear Evolution

In this section we consider nonlinear modes ($\gamma_{nl} \neq 0$) in the presence of lattice defects. For weak nonlinearity, with parameters similar to those considered above, nonlinear modes were found to exist in longitudinally driven

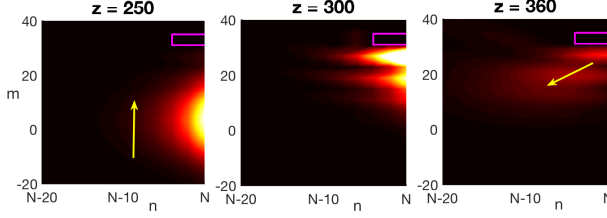


FIG. 14. Linear edge mode dynamics encountering a defect barrier in the Lieb lattice with the Floquet band positioned close to the bulk. Intensity evolution $|c_{mn}(z)|^2$ along straight edge for same rotation corresponding to the Floquet bands in Fig. 4(b) at $\alpha(2) = .191$.

honeycomb lattices [4, 18]. There it was found that the edge solitons ‘inherited’ the topological protection from the linear mode; we look to see if that is also the case here.

To begin, we introduce a small parameter that is related to the relatively rapid driving frequency $\epsilon = 1/\Omega \approx 0.239$. The weak nonlinearity scale is set to $\gamma_{nl} = \epsilon$. We next look for a soliton mode, which is a balance between dispersion and self-focusing nonlinearity. As such, we initialize these modes similar to (35) and (38) except we add an amplitude A coefficient in front of the sech terms that satisfies the balance $A^2\gamma_{nl} = \mu^2|\alpha''(\omega)|$. The full nonlinear Lieb (14)-(16) and Kagome (21)-(23) systems are then evolved in z .

In Fig. 16 we show two *nonlinear* topologically protected modes: one Lieb and one Kagome using the same parameters taken in Figs. 13 and 15 along the straight edge. Using the balance given above, the nonlinear modes are found to closely mirror the unidirectional behavior of the linear states. Namely, for edge modes whose Floquet exponent is deep in the gap and Floquet band is slope-definite throughout the gap, we observe scatter-free propagation. When the mode is not deep in the gap or the sign of the group velocity depends on ω the mode can scatter backward (see Figs. 14 and 15). These nonlinear states are appealing since they appear to combine topologically protected one-way motion with the robustness and balance of solitons.

V. CONCLUSIONS

Tight-binding approximations were given that describe deep longitudinally driven Lieb and Kagome waveguide lattices. These lattices were decomposed into three sub-lattices each of which was given its own driving pattern e.g. phase offset, different radii, different frequency, etc. We considered periodically oscillating waveguides and computed their corresponding Floquet bands. These dispersion bands were found to support localized edge modes that were either stationary (flat band) or traveling.

Edge modes located in the band gap with sign-definite group velocity throughout the gap were found to propagate unidirectionally around lattice defect barriers, and

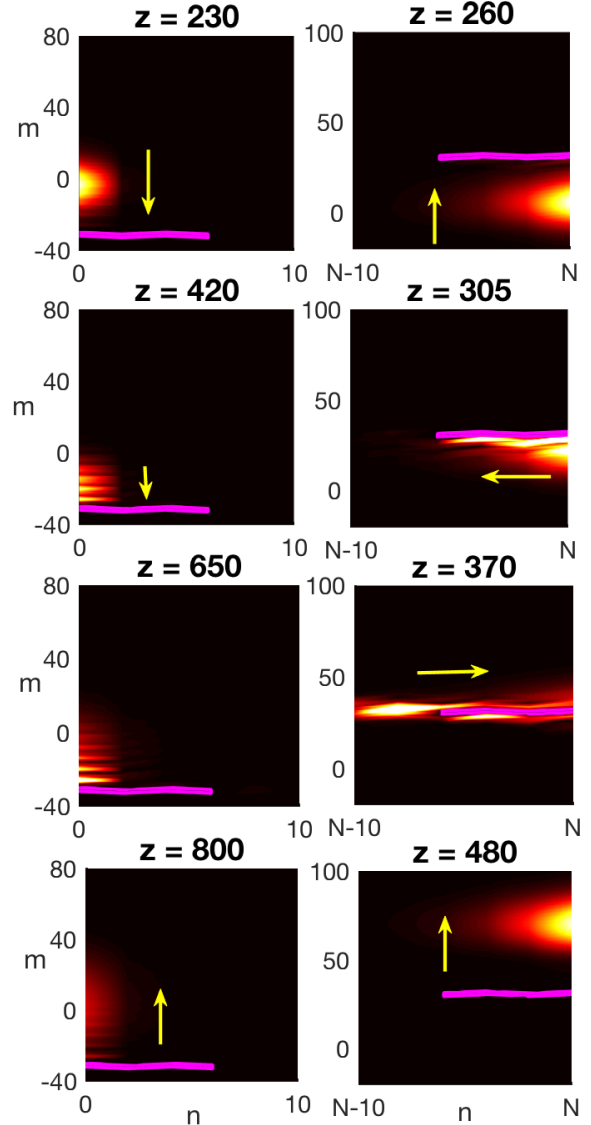


FIG. 15. Linear edge mode dynamics encountering a defect barrier in the Kagome lattice for in-phase rotation corresponding to the Floquet bands in Fig. 10(b) with $\omega = 1.2$. (Left column) Intensity evolution $|b_{mn}(z)|^2$ along pointy edge with same rotation. (Right column) Intensity evolution $|c_{mn}(z)|^2$ along straight edge.

did not significantly backscatter; indicating they are topologically protected modes. If, on the other hand, the corresponding Floquet band has sign-indefinite group velocity, then the edge mode could backscatter at the barrier. Additionally, when the corresponding Floquet exponent was not well-separated from the bulk band, then scattering could occur.

Two important conclusions can be drawn from this work: (i) Numerous lattices can be used to find topologically protected edge modes e.g. honeycomb, square, Lieb, Kagome, etc. The tight-binding approach we have developed can be generalized to incorporate even more detailed models e.g. next-nearest neighbor interaction, detuning in the refractive index etc. (ii) Many different

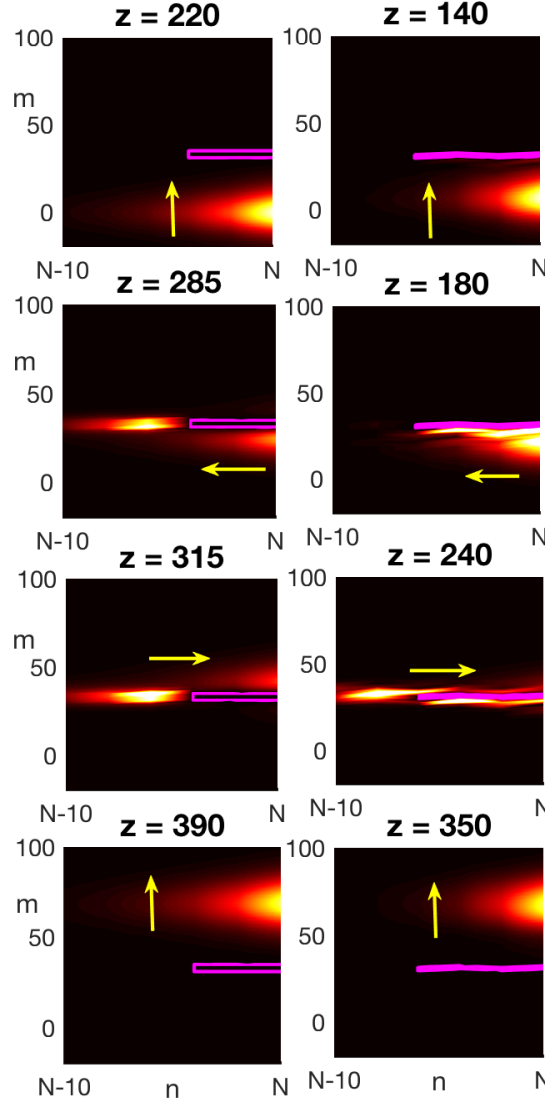


FIG. 16. Nonlinear ($\gamma_{nl} = \epsilon = 1/\Omega$) edge mode dynamics encountering a defect barrier. (Left column) Intensity, $|c_{mn}(z)|^2$, in Lieb lattice with same parameters as those given in right column of Fig. 13 with dispersion $\alpha''(1.65) = -0.0364$ corresponding to Fig. 4(b). (Right column) Intensity, $|c_{mn}(z)|^2$, in Kagome lattice with same parameters as those given in right column of Fig. 15 with dispersion $\alpha''(1.2) = .141$ corresponding to Fig. 10(b).

types of longitudinal driving can generate unidirectional and bi-directional edge modes. Different rotation patterns can be selected to suit the needs of the task e.g. along the bearded edge of a Lieb lattice π -offset rotation creates faster moving modes than in-phase rotation.

Finally, weakly nonlinear modes were found to inherit the topological protection of the linear Floquet modes. These modes present an exciting opportunity to merge the one-way properties of the linear problem with intense nonlinear states i.e. solitons.

VI. ACKNOWLEDGEMENTS

This work was partially supported by AFOSR under grant No. FA9550-16-1-0041.

[1] F. Haldane and S. Raghu, Phys. Rev. Lett. **100**, 013904 (2008).
[2] Z. Wang, Y. Chong, J. Joannopoulos, and Soljačić, Nature **461**, 772 (2009).
[3] M. C. Rechtsman, J. M. Zeuner, Y. Plotnik, Y. Lumer, S. Nolte, F. Dreisow, M. Segev, and A. Szameit, Nature **496**, 196 (2013).
[4] M. J. Ablowitz and J. T. Cole, Phys. Rev. A **96**, 043868 (2017).
[5] D. Leykam, M. C. Rechtsman, and Y. D. Chong, Phys. Rev. Lett. **117**, 013902 (2016).
[6] D. Leykam and Y. D. Chong, Phys. Rev. Lett. **117**, 143901 (2016).
[7] J. Noh, S. Huang, D. Leykam, Y. D. Chong, K. P. Chen, and M. C. Rechtsman, Nature Physics **13**, 611 (2017).
[8] Y. Lumer, M. C. Rechtsman, Y. Plotnik, and M. Segev, Phys Rev A **94**, 021801(R) (2016).
[9] M. A. Bandres, M. C. Rechtsman, and M. Segev, Phys. Rev. X **6**, 011016 (2016).
[10] X. Zhou, Y. Wang, D. Leykam, and Y. D. Chong, New J. Phys. **19**, 095002 (2017).
[11] R. El-Ganainy and M. Levy, Opt. Lett. **40**, 5275 (2015).

- [12] W. Qiu, Z. Wang, and M. Soljačić, Opt. Express **19**, 22248 (2011).
- [13] B. Bahari, A. Nda, F. Vallini, A. El Amili, Y. Fainman, and B. Kanté, Science (2017).
- [14] P. St-Jean, V. Goblot, E. Galopin, A. Lemaître, T. Ozawa, L. Le Gratiet, I. Sagnes, J. Bloch, and A. Amo, Nature Photonics **11**, 651 (2017).
- [15] M. Parto, S. Wittek, H. Hodaei, G. Harari, M. A. Bandres, J. Ren, M. C. Rechtsman, M. Segev, D. N. Christodoulides, and M. Khajavikhan, ArXiv:1709.00523v1 (2017).
- [16] M. A. Bandres, S. Wittek, G. Harari, M. Parto, J. Ren, M. Segev, D. N. Christodoulides, and M. Khajavikhan, Science (2018).
- [17] G. Harari, M. A. Bandres, Y. Lumer, M. C. Rechtsman, Y. D. Chong, M. Khajavikhan, D. N. Christodoulides, and M. Segev, Science (2018).
- [18] M. J. Ablowitz, C. Curtis, and Y.-P. Ma, Phys. Rev. A **90**, 023813 (2014).
- [19] D. Guzmán-Silva, C. Mejía-Cortés, M. A. Bandres, M. Rechtsman, S. Weimann, S. Nolte, M. Segev, A. Szameit, and R. A. Vicencio, New J. Phys. **16**, 063061 (2014).
- [20] R. A. Vicencio, C. Cantillano, L. Morales-Inostroza, B. Real, C. Mejía-Cortés, S. Weimann, A. Szameit, and M. I. Molina, Phys. Rev. Lett. **114**, 245503 (2015).
- [21] S. Mukherjee, A. Spracklen, D. Choudhury, N. Goldman, P. Öhberg, E. Andersson, and R. R. Thomson, Phys. Rev. Lett. **114**, 245504 (2015).
- [22] Y. Zong, S. Xia, L. Tang, D. Song, Y. Hu, Y. Pei, J. Su, Y. Li, and Z. Chen, Opt. Express **24**, 8877 (2016).
- [23] M. A. Bandres, M. C. Rechtsman, A. Szameit, and M. Segev, CLEO:2014 OSA Technical Digest , FF2D.3 (2014).
- [24] R. A. Vicencio and C. Mejía-Cortés, J. Opt. **16**, 015706 (2014).
- [25] A. Szameit and S. Nolte, J. Phys. B: At. Mol. Opt. Phys. **43**, 163001 (2010).

Appendix A: Floquet Bands for Honeycomb and Staggered Square Lattices

In our studies we have observed that quite often similar sublattice driving patterns often yield similar Floquet bands, regardless of the underlying lattice. To emphasize this point we will show typical dispersion bands for the honeycomb and staggered square lattices [4] for rotation parameters similar to those considered above. These lattices possess two lattice sites per unit cell, unlike the three lattice sites per unit cell for Lieb and Kagome. In terms of the discrete system given in Sec. II, these simpler systems can be described within the Lieb/Kagome framework by taking $a_{mn}(z) = 0$. We take the rotating frame to co-move with the b lattice site and only the c sites interact with it.

The Floquet bands for the honeycomb lattice are shown in Fig. 17. The parameters are identical to those used in Fig. 11. Topologically protected traveling modes are observed in the case of different radii [Fig. 17(b)], different frequency [Fig. 17(c)], π -offset [Fig. 17(d)] and quasi 1d motion [Fig. 17(f)]. The edge modes found in

the case of counter rotation [see Fig. 17(e)] do not travel i.e. $\alpha'(\omega) = 0$. Similar to the Lieb and Kagome lattices, the π -offset rotation has an additional family of solutions located at the Floquet edge. Similar to the Kagome lattice [see Fig. 11(a)], the honeycomb lattice possesses non-topological (bi-directional) modes in the case of anisotropy [see Fig. 17(a)]. The modes for quasi 1d motion are found to travel in propagate in the opposite direction relative to all other rotation patterns, just like the Lieb, Kagome and square lattices (see below).

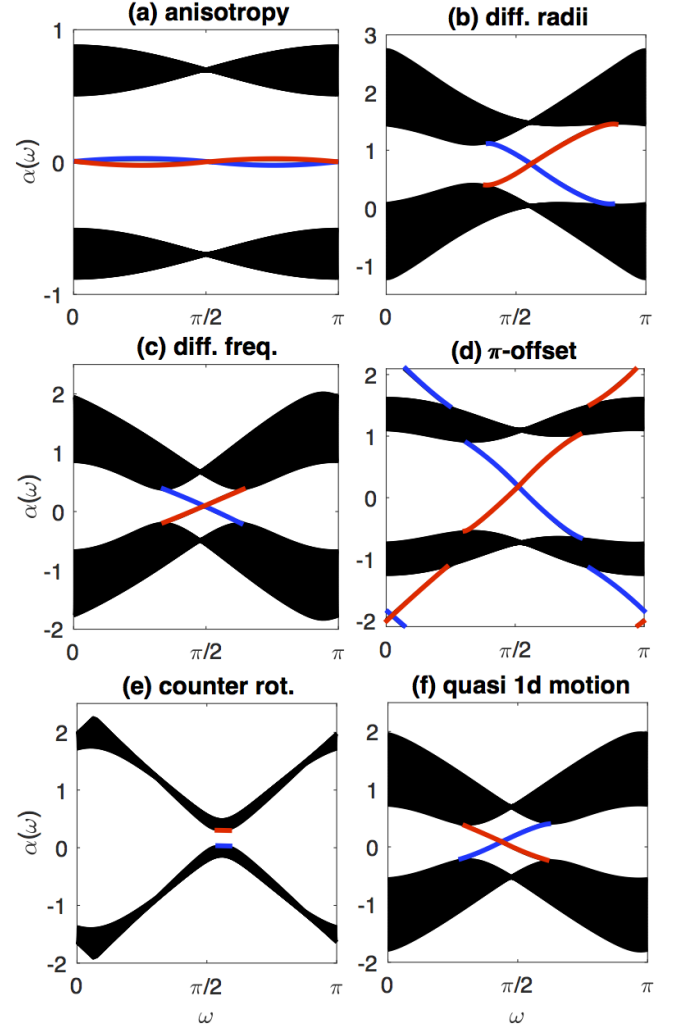


FIG. 17. (Color online) Honeycomb Floquet bands for various rotation patterns with zig-zag boundary conditions. Red curves indicate edge modes on right edge, blue curves denote left edge modes. The parameters used are the same as in Fig. 11 with $a_{mn}(z) = 0$.

The next set of band diagrams are for the staggered square lattice (see Fig. 18). In this case the underlying lattice is actually simple. As a result, for same rotation with anisotropic waveguides we obtain the bands in Fig. 18(a) that do not support any edge modes. However, by driving two sublattices in different patterns, topological edge modes can be generated. Traveling uni-

directional/topological modes are generated by different radii [Fig. 18(b)], different frequency [Fig. 18(c)], π -offset [Fig. 18(d)], counter rotation [Fig. 18(e)], and quasi 1d motion [Fig. 18(f)]. Like each other case above, the π -offset rotation pattern has a radius threshold necessary to generate the modes shown in Fig. 18(d). Additional modes are found near Floquet center ($\alpha = 0$) (or central band gap) for different radii, counter rotation, and quasi 1d motion, unlike the honeycomb lattice above. Similar to the Lieb, Kagome, and honeycomb lattices, modes generated from the quasi 1d motion bands propagate in an opposite orientation, relative to most other cases.

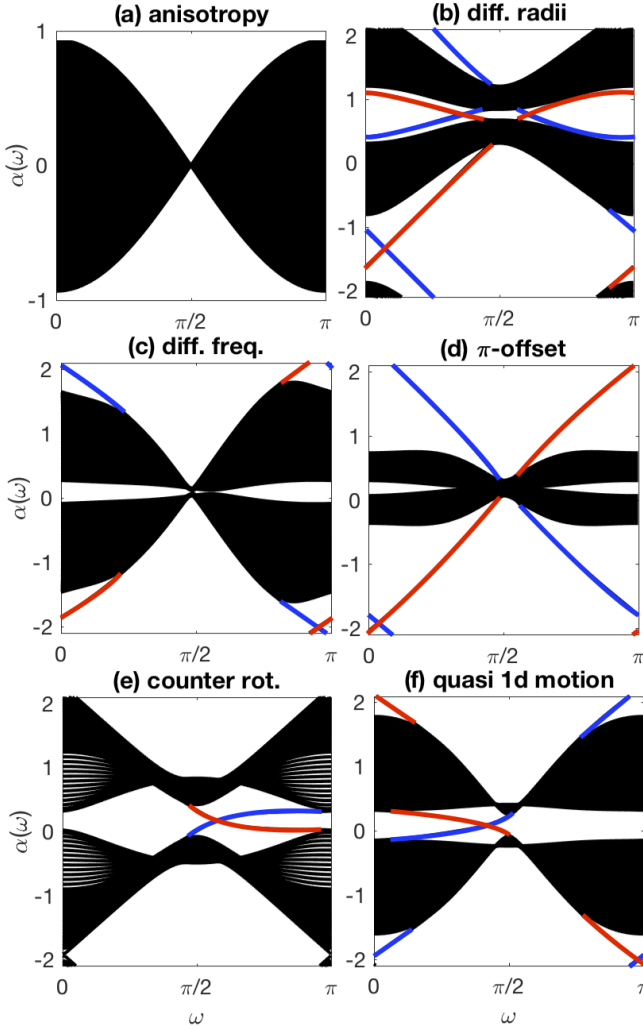


FIG. 18. (Color online) Staggered square Floquet bands for various rotation patterns. Red curves indicate edge modes on right edge, blue curves denote left edge modes. The parameters used are the same as in Fig. 11 with $a_{mn}(z) = 0$.

same coefficients. The only difference in the two tight-binding models is the individual lattice configurations i.e. the different lattice vectors between nearest neighbor lattice sites, and which interactions are taking into account. We emphasize again that our approach is quite general and can be adapted to other longitudinally driven waveguide arrays.

The linear coefficients in our tight-binding approximations are

$$\begin{aligned} \mathbb{L}(\mathbf{v} - \Delta \mathbf{h}_{ij}(z)) = & \left[V_0^3 \sqrt{\frac{\sigma_x \sigma_y}{(1 + \sigma_x V_0)(1 + \sigma_y V_0)}} \right. \\ & \times \left(2e^{-\frac{V_0}{4} \left[\frac{[\mathbf{v} - \Delta \mathbf{h}_{ij}(z)]_x^2}{\sigma_x(1 + V_0 \sigma_x)} + \frac{[\mathbf{v} - \Delta \mathbf{h}_{ij}(z)]_y^2}{\sigma_y(1 + V_0 \sigma_y)} \right]} - 1 \right) \\ & + \frac{V_0^2}{4} \left(\frac{[\mathbf{v} - \Delta \mathbf{h}_{ij}(z)]_x^2}{\sigma_x^2} + \frac{[\mathbf{v} - \Delta \mathbf{h}_{ij}(z)]_y^2}{\sigma_y^2} \right) \\ & \left. \times e^{-\frac{V_0}{4} \left(\frac{[\mathbf{v} - \Delta \mathbf{h}_{ij}(z)]_x^2}{\sigma_x} + \frac{[\mathbf{v} - \Delta \mathbf{h}_{ij}(z)]_y^2}{\sigma_y} \right)} e^{i\mathbf{v} \cdot (\mathbf{k} + \mathbf{A}(z))} \right], \end{aligned}$$

and

$$\begin{aligned} \mathbb{R}(\mathbf{v} - \Delta \mathbf{h}_{ij}(z)) = & \frac{V_0}{2} \left[\frac{[\Delta \mathbf{h}'_{2j}(z) \cdot (\mathbf{v} - \Delta \mathbf{h}_{ij}(z))]_x}{\sigma_x} \right. \\ & + \left. \frac{[\Delta \mathbf{h}'_{2j}(z) \cdot (\mathbf{v} - \Delta \mathbf{h}_{ij}(z))]_y}{\sigma_y} \right] \\ & \times e^{-\frac{V_0}{4} \left(\frac{[\mathbf{v} - \Delta \mathbf{h}_{ij}(z)]_x^2}{\sigma_x} + \frac{[\mathbf{v} - \Delta \mathbf{h}_{ij}(z)]_y^2}{\sigma_y} \right)} e^{i\mathbf{v} \cdot (\mathbf{k} + \mathbf{A}(z))}, \end{aligned}$$

where the x and y subscripts denote the i and j components, respectively. Without loss of generality, we fix $\mathbf{k} = 0$ [18]. The nonlinearity coefficient for the tight-binding models is given by

$$\gamma_{\text{nl}} = \frac{\gamma V_0}{2\pi\sqrt{\sigma_x \sigma_y}} \geq 0.$$

The relative driving motion is captured by the functions $\Delta \mathbf{h}_{ij}(z) \equiv \mathbf{h}_i(z) - \mathbf{h}_j(z)$ and $\Delta \mathbf{h}'_{ij}(z) = \mathbf{h}'_i(z) - \mathbf{h}'_j(z)$ for $i, j = a, b, c$. The defining lattice vectors for the Lieb and Kagome lattices are given in Eq. (12) and (13), respectively.

Appendix B: Tight-binding Model Coefficients

The coefficients in the tight-binding models given in Sec. II are presented here. Both the Lieb (14)-(16) and Kagome (21)-(23) systems are defined in terms of the